PASSAGE OF PARTICLES THROUGH MATTER

To reduce the size of this section's PostScript file, we have divided it into three PostScript files. We present the following index:

PART 1

PART 2

PART 3

23.3. Multiple scattering through small angles

A charged particle traversing a medium is deflected by many small-angle scatters. Most of this deflection is due to Coulomb scattering from nuclei, and hence the effect is called multiple Coulomb scattering. (However, for hadronic projectiles, the strong interactions also contribute to multiple scattering.) The Coulomb scattering distribution is well represented by the theory of Molière [29]. It is roughly Gaussian for small deflection angles, but at larger angles (greater than a few θ_0, defined below) it behaves like Rutherford scattering, having larger tails than does a Gaussian distribution.

If we define

$$\theta_0 = \theta^{\rm rms}_{\rm plane} = \frac{1}{\sqrt{2}}\,\theta^{\rm rms}_{\rm space}\ . \tag{23.8}$$

then it is sufficient for many applications to use a Gaussian approximation for the central 98% of the projected angular distribution, with a width given by [30,31]

$$\theta_0 = \frac{13.6\ {\rm MeV}}{\beta cp}\ z\ \sqrt{x/X_0}\Big[1 + 0.038\ln(x/X_0)\Big]\ . \tag{23.9}$$

Here p, βc, and z are the momentum, velocity, and charge number of the incident particle, and x/X_0 is the thickness of the scattering medium in radiation lengths (defined below). This value of θ_0 is from a fit to Molière distribution [29] for singly charged particles with $\beta = 1$ for all Z, and is accurate to 11% or better for $10^{-3} < x/X_0 < 100$.

Eq. (23.9) describes scattering from a single material, while the usual problem involves the multiple scattering of a particle traversing many different layers and mixtures. Since it is from a fit to a Molière distribution, it is incorrect to add the individual θ_0 contributions in quadrature; the result is systematically too small. It is much more accurate to apply Eq. (23.9) once, after finding x and X_0 for the combined scatterer.

Lynch and Dahl have extended this phenomenological approach, fitting Gaussian distributions to a variable fraction of the Molière distribution for arbitrary scatterers [31], and achieve accuracies of 2% or better.

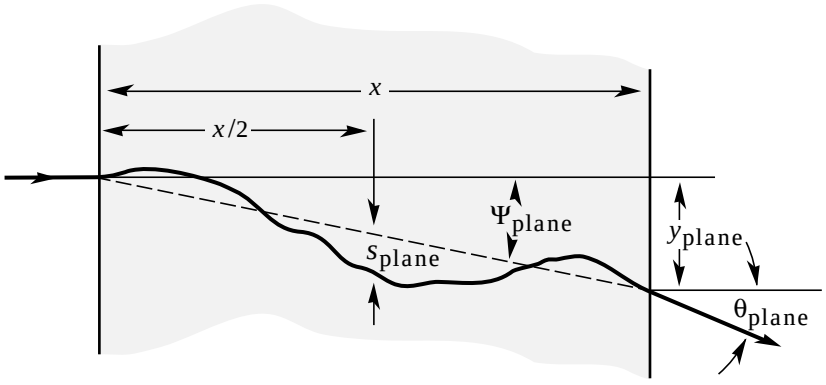

Figure 23.5: Quantities used to describe multiple Coulomb scattering. The particle is incident in the plane of the figure.

The nonprojected (space) and projected (plane) angular distributions are given approximately by [29]

$$\frac{1}{2\pi\,\theta_0^2}\,\exp\left(-\frac{\theta^2_{\rm space}}{2\theta_0^2}\right)\,d\Omega\ , \tag{23.10}$$

$$\frac{1}{\sqrt{2\pi}\,\theta_0}\,\exp\left(-\frac{\theta^2_{\rm plane}}{2\theta_0^2}\right)\,d\theta_{\rm plane}\ , \tag{23.11}$$

where θ is the deflection angle. In this approximation, $\theta^2_{\rm space} \approx (\theta^2_{{\rm plane},x} + \theta^2_{{\rm plane},y})$, where the x and y axes are orthogonal to the direction of motion, and $d\Omega \approx d\theta_{{\rm plane},x}\,d\theta_{{\rm plane},y}$. Deflections into $\theta_{{\rm plane},x}$ and $\theta_{{\rm plane},y}$ are independent and identically distributed.

Figure 23.5 shows these and other quantities sometimes used to describe multiple Coulomb scattering. They are

$$\psi^{\,\rm rms}_{\rm plane} = \frac{1}{\sqrt{3}}\,\theta^{\,\rm rms}_{\rm plane} \quad = \frac{1}{\sqrt{3}}\,\theta_0\ , \tag{23.12}$$

$$y^{\,\rm rms}_{\rm plane} = \frac{1}{\sqrt{3}}\,x\,\theta^{\,\rm rms}_{\rm plane} \ = \frac{1}{\sqrt{3}}\,x\,\theta_0\ , \tag{23.13}$$

$$s^{\,\rm rms}_{\rm plane} = \frac{1}{4\sqrt{3}}\,x\,\theta^{\,\rm rms}_{\rm plane} = \frac{1}{4\sqrt{3}}\,x\,\theta_0\ . \tag{23.14}$$

All the quantitative estimates in this section apply only in the limit of small $\theta^{\,\rm rms}_{\rm plane}$ and in the absence of large-angle scatters. The random variables s, ψ, y, and θ in a given plane are distributed in a correlated fashion (see Sec. 28.1 of this *Review* for the definition of the correlation coefficient). Obviously, $y \approx x\psi$. In addition, y and θ have the correlation coefficient $\rho_{y\theta} = \sqrt{3}/2 \approx 0.87$. For Monte Carlo generation of a joint $(y_{\rm\,plane}, \theta_{\rm plane})$ distribution, or for other calculations, it may be most convenient to work with independent Gaussian random variables (z_1, z_2) with mean zero and variance one, and then set

$$\begin{aligned} y_{\rm plane} =& z_1\,x\,\theta_0(1-\rho^2_{y\theta})^{1/2}/\sqrt{3} + z_2\,\rho_{y\theta}x\,\theta_0/\sqrt{3} \\ =& z_1\,x\,\theta_0/\sqrt{12} + z_2\,x\,\theta_0/2\ ; \end{aligned} \tag{23.15}$$

$$\theta_{\rm plane} = z_2\,\theta_0\ . \tag{23.16}$$

Note that the second term for $y_{\rm\,plane}$ equals $x\,\theta_{\rm plane}/2$ and represents the displacement that would have occurred had the deflection $\theta_{\rm plane}$ all occurred at the single point $x/2$.

For heavy ions the multiple Coulomb scattering has been measured and compared with various theoretical distributions [32].

23.4. Radiation length and associated quantities

In dealing with electrons and photons at high energies, it is convenient to measure the thickness of the material in units of the radiation length X_0. This is the mean distance over which a high-energy electron loses all but $1/e$ of its energy by bremsstrahlung, and is the appropriate scale length for describing high-energy electromagnetic cascades. X_0 has been calculated and tabulated by Y.S. Tsai [33]:

$$\frac{1}{X_0} = 4\alpha r_e^2 \frac{N_A}{A}\Big\{ Z^2\big[L_{\rm rad} - f(Z)\big] + Z\,L'_{\rm rad}\Big\} \ . \tag{23.17}$$

For $A = 1$ g mol^{-1}, $4\alpha r e^2 N_A/A = (716.408 \text{ g cm}^{-2})^{-1}$. $L_{\rm rad}$ and $L'_{\rm rad}$ are given in Table 23.2. The function $f(Z)$ is an infinite sum, but for elements up to uranium can be represented to 4-place accuracy by

$$f(Z) = a^2\big[(1+a^2)^{-1} + 0.20206 \\ -0.0369\,a^2 + 0.0083\,a^4 - 0.002\,a^6\big] \ , \tag{23.18}$$

where $a = \alpha Z$ [34].

Table 23.2: Tsai's $L_{\rm rad}$ and $L'_{\rm rad}$, for use in calculating the radiation length in an element using Eq. (23.17).

Element	Z	$L_{\rm rad}$	$L'_{\rm rad}$
H	1	5.31	6.144
He	2	4.79	5.621
Li	3	4.74	5.805
Be	4	4.71	5.924
Others	> 4	$\ln(184.15\,Z^{-1/3})$	$\ln(1194\,Z^{-2/3})$

Although it is easy to use Eq. (23.17) to calculate X_0, the functional dependence on Z is somewhat hidden. Dahl provides a compact fit to the data [35]:

$$X_0 = \frac{716.4 \text{ g cm}^{-2}\,A}{Z(Z+1)\ln(287/\sqrt{Z})} \tag{23.19}$$

Results obtained with this formula agree with Tsai's values to better than 2.5% for all elements except helium, where the result is about 5% low.

The radiation length in a mixture or compound may be approximated by

$$1/X_0 = \sum w_j/X_j \ , \tag{23.20}$$

where w_j and X_j are the fraction by weight and the radiation length for the jth element.

An electron loses energy by bremsstrahlung at a rate nearly proportional to its energy, while the ionization loss rate varies only logarithmically with the electron energy. The *critical energy* E_c is sometimes defined as the energy at which the two loss rates are equal [36]. Berger and Seltzer [36] also give the approximation $E_c = (800 \text{ MeV})/(Z+1.2)$.

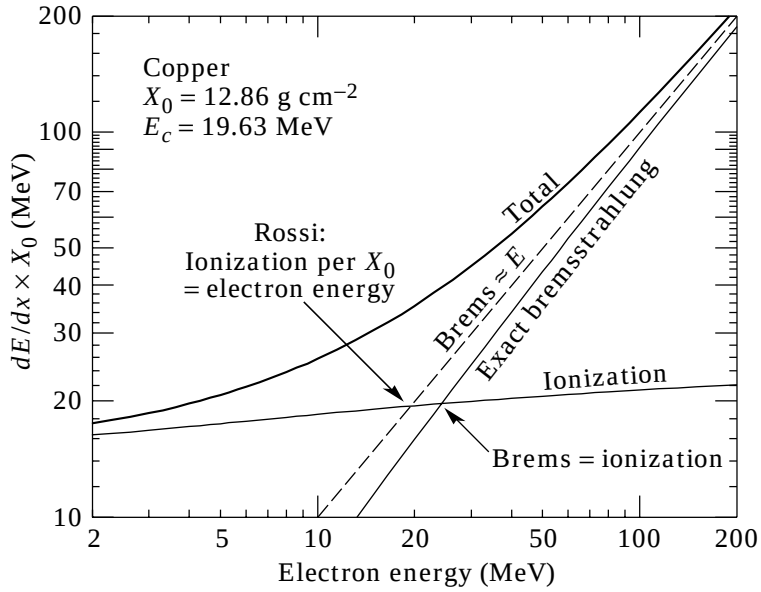

Figure 23.6: Two definitions of the critical energy E_c.

This formula has been widely quoted, and has been given in previous editions of this *Review* [23]. Among alternate definitions is that of Rossi [1], who defines the critical energy as the energy at which the ionization loss per radiation length is equal to the electron energy. Equivalently, it is the same as the first definition with the approximation $|dE/dx|_{\rm brems} \approx E/X_0$. These definitions are illustrated in the case of copper in Fig. 23.6.

The accuracy of approximate forms for E_c has been limited by the failure to distinguish between gases and solid or liquids, where there is a substantial difference in ionization at the relevant energy because of the density effect. We distinguish these two cases in Fig. 23.7. Fits were also made with functions of the form $a/(Z+b)^\alpha$, but α was essentially unity.

The transverse development of electromagnetic showers in different materials scales fairly accurately with the *Molière radius* R_M, given by [37,38]

$$R_M = X_0\, E_s/E_c \ , \tag{23.21}$$

where $E_s \approx 21$ MeV (see Table 23.1), and the Rossi definition of E_c is used.

In a material containing a weight fraction w_j of the element with critical energy E_{cj} and radiation length X_j, the Molière radius is given by

$$\frac{1}{R_M} = \frac{1}{E_s} \sum \frac{w_j\, E_{cj}}{X_j} \ . \tag{23.22}$$

For very high-energy photons, the total e^+e^- pair-production cross section is approximately

$$\sigma = \tfrac{7}{9}(A/X_0 N_A) \ , \tag{23.23}$$

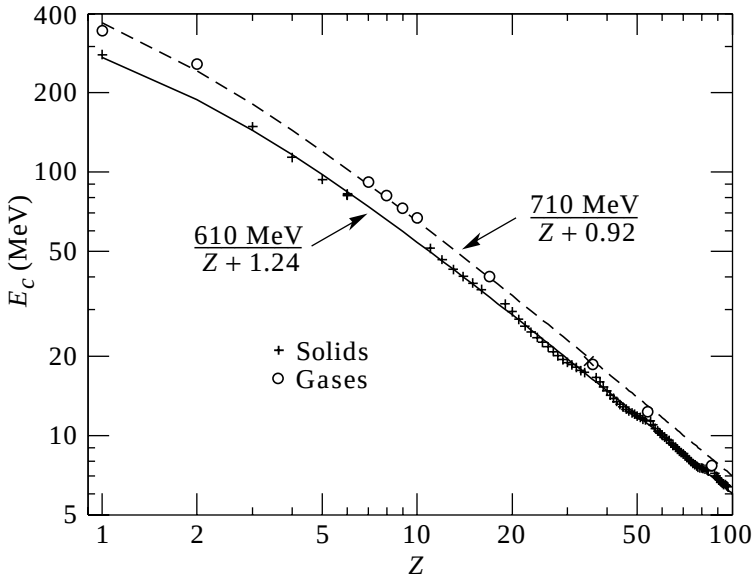

Figure 23.7: Electron critical energy for the chemical elements, using Rossi's definition [1]. The fits shown are for solids and liquids (solid line) and gases (dashed line). The rms deviation is 2.2% for the solids and 4.0% for the gases. (Computed with code supplied by A. Fassó.)

where A is the atomic weight of the material and N_A is Avogadro's number. Equation Eq. (23.23) is accurate to within a few percent down to energies as low as 1 GeV. The cross section decreases at lower energies, as shown in Fig. 24.4 of this *Review*. As the energy decreases, a number of other processes become important, as is shown in Fig. 24.3 of this *Review*.

23.5. Electromagnetic cascades

When a high-energy electron or photon is incident on a thick absorber, it initiates an electromagnetic cascade as pair production and bremsstrahlung generate more electrons and photons with lower energy. The longitudinal development is governed by the high-energy part of the cascade, and therefore scales as the radiation length in the material. Electron energies eventually fall below the critical energy, and then dissipate their energy by ionization and excitation rather than by the generation of more shower particles. In describing shower behavior, it is therefore convenient to introduce the scale variables

$$t = x/X_0$$
$$y = E/E_c \ , \tag{23.24}$$

so that distance is measured in units of radiation length and energy in units of critical energy.

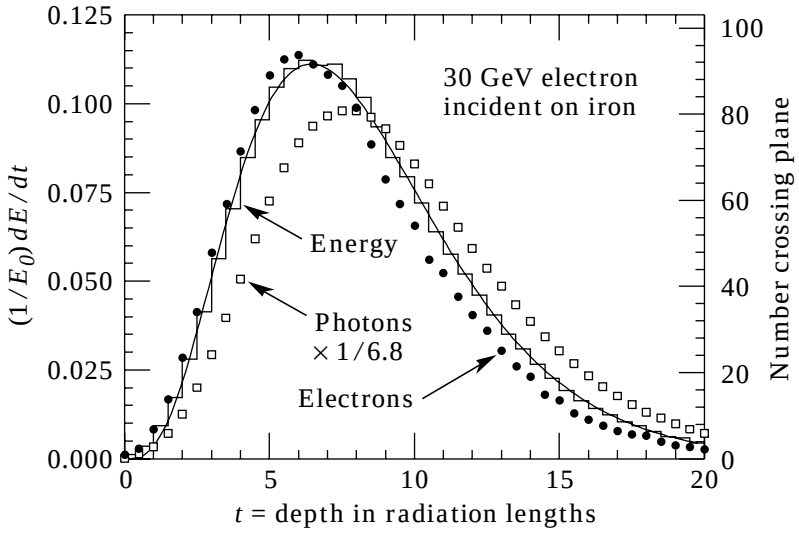

Figure 23.8: An EGS4 simulation of a 30 GeV electron-induced cascade in iron. The histogram shows fractional energy deposition per radiation length, and the curve is a gamma-function fit to the distribution. Circles indicate the number of electrons with total energy greater than 1.5 MeV crossing planes at $X_0/2$ intervals (scale on right) and the squares the number of photons with $E \geq 1.5$ MeV crossing the planes (scaled down to have same area as the electron distribution).

Longitudinal profiles for an EGS4 [22] simulation of a 30 GeV electron-induced cascade in iron are shown in Fig. 23.8. The number of particles crossing a plane (very close to Rossi's Π function [1]) is sensitive to the cutoff energy, here chosen as a total energy of 1.5 MeV for both electrons and photons. The electron number falls off more quickly than energy deposition. This is because, with increasing depth, a larger fraction of the cascade energy is carried by photons. Exactly what a calorimeter measures depends on the device, but it is not likely to be exactly any of the profiles shown. In gas counters it may be very close to the electron number, but in glass Čerenkov detectors and other devices with "thick" sensitive regions it is closer to the energy deposition (total track length). In such detectors the signal is proportional to the "detectable" track length T_d, which is in general less than the total track length T. Practical devices are sensitive to electrons with energy above some detection threshold E_d, and $T_d = T\,F(E_d/E_c)$. An analytic form for $F(E_d/E_c)$ obtained by Rossi [1] is given by Fabjan [39]; see also Amaldi [40].

The mean longitudinal profile of the energy deposition in an electromagnetic cascade is reasonably well described by a gamma distribution [41]:

$$\frac{dE}{dt} = E_0\, b\, \frac{(bt)^{a-1}\, e^{-bt}}{\Gamma(a)} \tag{23.25}$$

The maximum $t_{\rm max}$ occurs at $(a-1)/b$. We have made fits to shower profiles in elements ranging from carbon to uranium, at energies from 1 GeV to 100 GeV. The energy

deposition profiles are well described by Eq. (23.25) with

$$t_{\max} = (a-1)/b = 1.0 \times (\ln y + C_j) \ , \qquad j = e, \gamma \ , \tag{23.26}$$

where $C_e = -0.5$ for electron-induced cascades and $C_\gamma = +0.5$ for photon-induced cascades. To use Eq. (23.25), one finds $(a-1)/b$ from Eq. (23.26) and Eq. (23.24), then finds a either by assuming $b \approx 0.5$ or by finding a more accurate value from Fig. 23.9. The results are very similar for the electron number profiles, but there is some dependence on the atomic number of the medium. A similar form for the electron number maximum was obtained by Rossi in the context of his "Approximation B," [1] (see Fabjan's review in Ref. 39), but with $C_e = -1.0$ and $C_\gamma = -0.5$; we regard this as superseded by the EGS4 result.

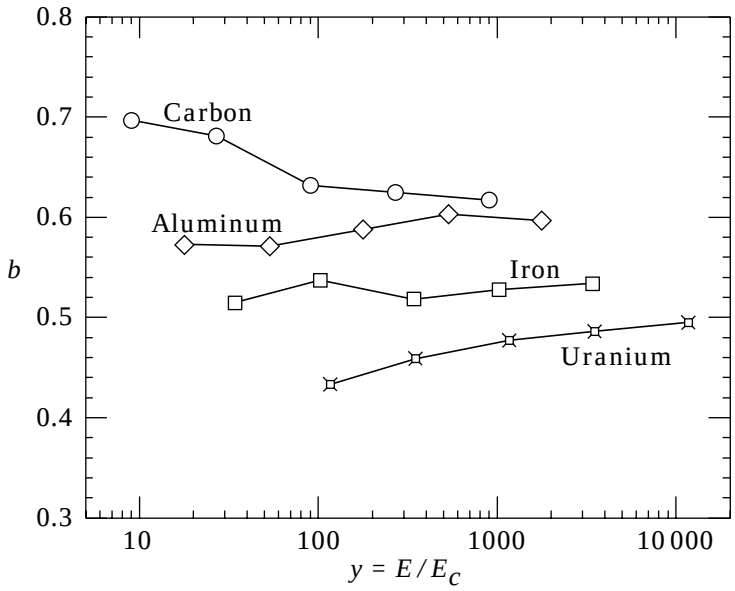

Figure 23.9: Fitted values of the scale factor b for energy deposition profiles obtained with EGS4 for a variety of elements for incident electrons with $1 \leq E_0 \leq 100$ GeV. Values obtained for incident photons are essentially the same.

The "shower length" $X_s = X_0/b$ is less conveniently parameterized, since b depends upon both Z and incident energy, as shown in Fig. 23.9. As a corollary of this Z dependence, the number of electrons crossing a plane near shower maximum is underestimated using Rossi's approximation for carbon and seriously overestimated for uranium. Essentially the same b values are obtained for incident electrons and photons. For many purposes it is sufficient to take $b \approx 0.5$.

The gamma distribution is very flat near the origin, while the EGS4 cascade (or a real cascade) increases more rapidly. As a result Eq. (23.25) fails badly for about the first two radiation lengths; it was necessary to exclude this region in making fits.

Because fluctuations are important, Eq. (23.25) should be used only in applications where average behavior is adequate. Grindhammer *et al.* have developed fast simulation algorithms in which the variance and correlation of a and b are obtained by fitting Eq. (23.25) to individually simulated cascades, then generating profiles for cascades using a and b chosen from the correlated distributions [42].

Measurements of the lateral distribution in electromagnetic cascades are shown in Refs. 37 and 38. On the average, only 10% of the energy lies outside the cylinder with radius R_M. About 99% is contained inside of $3.5R_M$, but at this radius and beyond composition effects become important and the scaling with R_M fails. The distributions are characterized by a narrow core, and broaden as the shower develops. They are often represented as the sum of two Gaussians, and Grindhammer [42] describes them with the function

$$f(r) = \frac{2r\,R^2}{(r^2 + R^2)^2}\ , \tag{23.27}$$

where R is a phenomenological function of x/X_0 and $\ln E$.